Article type: Original Paper

Mie-resonant membrane Huygens' metasurfaces

Quanlong Yang, Sergey Kruk, Yuehong Xu, Qingwei Wang, Yogesh Kumar Srivastava, Kirill Koshelev, Ivan Kravchenko, Ranjan Singh, Jiaguang Han*, Yuri Kivshar, and Ilya Shadrivov*

*Corresponding authors: E-mail: ilya.shadrivov@anu.edu.au; jiaghan@tju.edu.cn;

Dr. Q. Yang, Dr. S. Kruk, K. Koshelev, Prof. Y. Kivshar and Prof. I. Shadrivov
Nonlinear Physics Centre, Australian National University, Canberra ACT 2601, Australia

Dr. Q. Yang, Y. Xu, Q. Wang, and Prof. J. Han
Center for Terahertz Waves, Tianjin University, Tianjin 300072, China

Dr. Y. K. Srivastava, Prof. R. Singh
Division of Physics and Applied Physics, School of Physical and Mathematical Sciences, Nanyang Technological University, Singapore 637371, Singapore

Dr. Y. K. Srivastava, Prof. R. Singh
Centre for Disruptive Photonic Technologies, The Photonics Institute, Nanyang Technological University, Singapore 637371, Singapore

Dr. I. Kravchenko
Center for Nanophase Materials Sciences, Oak Ridge National Laboratory, TN 37831, USA

All-dielectric metasurfaces became a new paradigm for flat optics as they allow flexible engineering of the electromagnetic space of propagating waves. Such metasurfaces are usually composed of individual subwavelength elements embedded into a host medium or placed on a substrate, which often diminishes the quality of the resonances. The substrate imposes limitations on the metasurface functionalities, especially for infrared and terahertz frequencies. Here we introduce a novel concept of membrane Huygens' metasurfaces. Our metasurfaces feature an inverted design, and they consist of arrays of holes made in a thin membrane of high-index dielectric material, with the response governed by the electric and magnetic Mie resonances excited within dielectric domains of the membrane. We demonstrate highly efficient transmission combined with the 2π phase coverage in the free-standing membranes. We design several functional metadevices for the wavefront control, including beam deflector, a lens and an axicon. Such membrane metasurfaces provide novel opportunities for efficient large-area metadevices.

Metasurfaces with planar subwavelength resonators have been established as a route to control the electromagnetic waves in spectral ranges varying from microwaves to visible light.[1-9] First designs of metasurfaces mostly involved metallic plasmonic elements.[10-14] However, recent studies have demonstrated that the high-index dielectric nanoparticles bring a more efficient alternative design via low-order dipole and multipole Mie resonances.[15-17] Indeed, with very low intrinsic losses of Mie resonators supporting overlapping electric and magnetic multipoles, all-dielectric metasurfaces provide access to various flat-optics manipulations with great performance, such as imaging,[18] holography,[19] polarization control,[20] quantum tomography,[21] and biosensing.[22] Such planar structures with optimized high transmission based on Kerker effect are often termed as Huygens' metasurfaces.[23-25]

A typical building block of a dielectric metasurface is a subwavelength resonator made of a high-index dielectric material embedded into a low-index environment, e.g., a nanodisk placed on a low-index substrate. However, the overall efficiency of a metasurface composed of such resonators is strongly affected by the contrast of refractive indices of the resonator and substrate materials.[23] Even for low-index materials such as glass, the substrate would decrease the performance of the metadevice. Furthermore, in the terahertz (THz) frequency range, the substrate thickness is usually comparable with the wavelength of the THz radiation, which thus results in additional interference effects (such as etalon effect).

The essence of the membrane metasurface we suggest and demonstrate here is a thin planar structure consisting of low-index (*e.g.*, air) holes made in a high-index (*e.g.,* silicon) wafer is illustrated in **Figure 1**a. Being different from the conventional Mie resonators, the proposed free-standing structured membrane look similar to a photonic-crystal slab.[26-31] However*, in sharp contrast to photonic crystals* governed by the Bragg scattering from a periodically varying refractive index, the membrane metasurfaces feature a subwavelength

design, and their functionalities originate from the Mie scattering and Mie-resonant electric and magnetic localized modes.

We start from the multipole analysis of a dielectric Mie-resonant membrane metasurface - a silicon membrane suspended in air and perforated with circular holes (Figure 1b). For comparison, we also consider Huygens' metasurface with the more conventional design of dielectric disks (see the Supporting Information). We extract the transmission spectra and field profiles of the Mie resonances from the finite-element numerical analysis, and calculate the electric and magnetic dipole contributions to the total scattering cross-section for both silicon disk and membrane, by applying the multipole decomposition [32] (see the numerical simulation section). We find that in both the cases the optical response is dominated by the electric (ED) and magnetic (MD) dipole resonances with smaller contributions from higher-order multipole (HOM) modes. For nanodisks, two orthogonal ED and MD modes are located at the centers of the dielectric disks. Correspondingly, two ED and MD modes of the membrane metasurface are positioned in-between the holes, which are denoted by the red and blue arrows, respectively. Thus, most of the electromagnetic power is localized in the high-index silicon resonators created in the space between the neighboring holes.

To reveal the effect of the Mie resonant multipoles, we analyze the transmission profile and multipole decomposition versus the diameter of holes (Figure 1c). We find two transmission minima to match well with the position of the ED and MD resonances. When increasing the diameter, we identify ED and MD resonances overlapping at a specific critical diameter and separated for either larger or smaller diameters. Interestingly, the mode dispersion for the silicon membrane appears to be opposite to that of the disks. The lower-order mode for the large diameter of the holes is an electric dipole, while for disks it is a magnetic dipole. For the position of multipoles resonances, the electric and magnetic dipoles display a blueshift for the holes and a redshift for the disks. Such an inversion from the

conventional Mie scatterers by an interchange of dielectric disks by holes (e.g., areas of high-permittivity and low-permittivity materials) changes the positions of the electric and magnetic resonances, which displays some resemblance with the Babinet's principle.[30] The babinet's principle governs the electromagnetic response when transparent and non-transparent areas of the infinitesimally thin screens are interchanged. Then, we illustrate the normalized scattering cross-section of ED, MD and higher-order resonances (HOM) at the spectral overlap, which is shown in Figure 1d. In contrast to the case of separate resonances, we observe the close to unity transmission when the resonances overlap.

To quantitatively analyze the transmission and phase profile governed by the Mie resonances, we perform an experimental and numerical study of the transmission and phase spectra of the membrane metasurfaces with varying dimensions in the THz frequency range, which is displayed in **Figure 2**. Scalability of linear electromagnetic response makes it possible to extend our analysis and concepts to other frequency bands. It is worth noting that when the two resonances merge at a specific diameter (here D =132 μm), we observe that the transmission efficiency of the metasurface becomes as high as 90%, and the phase accumulation reaches full 2π, which is depicted by the two dashed lines in Figures 2a and 2b. In this case, the electric and magnetic resonances of the membrane metasurface are close to the spectral overlap at 1.15 THz. For other separate incidents, there exist two individual resonances with the maximum phase change of π. We fabricate the proposed structures and measure the transmission and phase spectra with a THz time-domain spectroscopy system. Figure 2b shows the experimental transmission and phase spectra of our dielectric membrane metasurface. We observe that the experimental data agree well with theory. In particular, we obtain the full 2π phase coverage, and observe the experimental transmission efficiency of membrane metasurfaces as high as 84.7%.

Next, we utilize the concept of membrane metasurfaces to demonstrate the wavefront control with non-uniform membrane metasurfaces. First, we design and fabricate a metasurface with a linear phase gradient thus acting as a beam deflector. We optimize the design for the bandwidth of our THz near-field scanning system around 0.77 THz. For this, we up-scale the design to 75 μm thickness and make corresponding diameter adjustments. We chose eight elements, all featuring high transmission with equidistant phase discretization over the 2π phase range for the full phase coverage (see the Supporting Information).

Figures 3a and 3b show the theoretical phase profile and optical image of the fabricated membrane deflector working at a target frequency of 0.77 THz. Here, the phase profile of membrane deflector could be estimated from: $\Delta\varphi = C_1 x$. C_1 is set to generate a phase gradient of 45°, x is the coordinate. First, we estimate the response of the membrane metasurface numerically. We show the numerically simulated electric field distribution of the membrane deflector (Figure 3c), and identify a uniform transmitted wave with a deflected angle of 11.8°. In the experiment, we use an angle-resolved THz time-domain spectroscopy system to characterize the performance of the metasurface (see the detailed angle-resolved THz system in the Experimental section). Figure 3d shows the measured angle-resolved transmission intensity spectra of the fabricated metasurface deflector, where most of the transmitted wave propagates along an angle deviated from the z-axis over the frequency ranging from 0.7 to 0.83 THz. We find that the deflected angle agrees well with the theoretical prediction. Notably, the performance of 0.77 THz denoted by the white dashed line in Figure 3d could be seen in Figure 3e and the measured defected angle is 11.2°. We also calculate the experimental diffraction efficiency of membrane deflector as a fraction of transmitted energy going into the required diffraction order, which is illustrated in Figure 3f, and we observe the best diffraction efficiency of up to 71.4% at 0.752 THz.

Next, we experimentally demonstrate the membrane metalens operating at 0.77 THz. We design the lens with a hyperbolic phase profile. the incident wave passing through the metasuface should meet a quadric phase relationship as below:

$$\Delta\varphi = \left(\sqrt{f^2 + r^2} - f\right)\frac{2\pi}{\lambda}, \tag{1}$$

where $\Delta\varphi$ is the phase difference between the positions at radius r and center point, f =12 mm is the focal length. Here the phase discretization is fulfilled by the chosen eight elements. The optical microscope images of the fabricated membrane metalens are presented in **Figure 4**a. The focusing can be seen from the numerical results of metalenses in the x-z plane in Figure 4b, where we observe that the focal length matches the design value. In the experiment, we employ a near-field scanning THz microscopy system to explore the field distribution of the designed membrane metalens (see the detail of the THz near-field scanning system in the Materials and Methods section). We observe an excellent agreement between the numerically simulated results and experimentally measured data at 0.79 THz (see Figure 4c), which clearly illustrates the beam focusing. Here, the shorter measured focal length comes from the fabrication error of the membrane thickness and possible misalignment of the incident THz wave (see the Supporting Information). The measured performance of metalenses beyond 0.79 THz further prove the broadband characteristics of the membrane metalens (see the Supporting Information).

Additionally, we measure focal spot profiles of the membrane metalens in the x-y plane, as shown in Figure 4d. The correponding phase profile is $\Delta\varphi = C_2 r$, and C_2 is a constant. Experimental results for the central focal beam show a perfect focusing effect matching well the numerical results. The ideal theoretical (red), numerical (green) and experimental (blue) cross-sections of the electric field of the membrane metalens (inset in Figure 4d) support our

conclusions. Besides the focusing ability, the performance of the membrane metasurface is also characterized by the transmission efficiency. The measured power efficiency of the metalens, in this case calculated as a fraction of the incident power reaching the focal spot, reaches 61.1 % at 0.79 THz.

Having demonstrated the wavefront control with a membrane metalens, next we demonstrate and analyze the performance of a membrane axicon with a phase profile of . **Figures 5**a and 5d show the phase profile and optical microscope images of the proposed meta-axicons. Here, the axicon has a linear phase gradient along the radial direction. We observe the generation of the Bessel beam by the meta-axicon, both numerically (Figure 5b) and experimentally (Figure 5e) at 0.83THz. The frequency deviation of membrane axicons comes from the thickness error of the fabricated silicon membrane. Being compared with an ideal Bessel beam in Figure 5e, the measured central beam and high-order diffraction in Figure 5f clearly illustrate the formation of the Bessel beam. The measured transmitted power of the meta-axicon is 54.9 % at 0.83 THz. The beam deflector, metalens, and meta-axicon confirm the suitability of the membrane metasurfaces for an even more sophisticated wavefront control.

In summary, we have suggested a novel concept for creating highly-efficient all-dielectric Huygens' metasurfaces based on membrane-type Mie-resonant dielectric structures. We have identified the conditions for overlapping the electric and magnetic dipole resonances in the membrane metasurface to realize highly efficient transmission with the demonstrated transmission efficiency of up to 84.7% and corresponding 2π phase coverage. To show the use of the concept of membrane metasurfaces, we further demonstrate the wavefront control with the membrane deflector, metalens, and metasurface axicons. Such membrane metasurfaces are more amenable to the fabrication with current commercial

micro/nanotechnology compared to their counterparts consisting of individual subwavelength resonators. This makes them a highly effective platform for flat-optic metadevices. At THz frequencies, our free-standing membrane devices solve a critical problem currently diminishing the efficiency of standard metasurfaces fabricated on substrates: they do not suffer from the etalon effect and have overall higher efficiency.

Experimental section

Numerical simulation: Numerical simulations are carried out using the finite-element frequency-domain solver of CST Microwave Studio. The silicon membrane with permittivity ε = 11.9 is suspended in air and perforated with cylindrical circular holes. The period of holes is P = 158 μm, and the thickness T = 50 μm. Unit cell boundary conditions are applied in both the x and y directions. The silicon disk array is surrounded by a benzocyclobutene (BCB) layer with a permittivity of ε = 2.7. The multipole decomposition is performed via COMSOL Multiphysics, the scattering cross-section of Mie multipoles is given by:

$$C_s = \frac{\pi}{k^2}\sum_{l=1}^{\infty}\sum_{m=-l}^{l}(2l+1)\left[\left|a_E(l,m)\right|^2+\left|a_M(l,m)\right|^2\right],$$

where a_E and a_M are the multipole coefficients coming from the distribution of the scattered electric field.

Fabrication: For the uniform structures, we start with a 50 μm free-standing silicon wafer. We deposit an 800 nm silicon oxide layer, and define the metasurface pattern on a photoresist

by standard photolithography. Then, we use inductively coupled plasma etching to etch the silicon oxide layer, that is then served as a mask for the deep reactive ion etching (DRIE) for perforating the silicon wafer. For the THz metadevices shown in Figs. 3-5, we start from silicon-on-insulator (SOI) wafers with a high-resistivity 75 µm device layer, 1µm buried oxide layer and 300 µm thick handle wafer. Both polished wafer sides are additionally covered with 1 micron of thermal silicon oxide. The metasurface pattern is delineated first in a photoresist which is used to transfer the metasurface shapes using reactive ion etching into the 1-micron thick silicon oxide layer which, in turn, served as a hard mask during deep reactive etching (DRIE) of the device layer. The residuals of the mask were left on the samples after etching. The resulting metasurface in the device layer was passivated by 1.4-micron thick silicon oxide deposited using plasma-enhanced chemical vapor deposition (PECVD) to provide the device membrane with protection and mechanical strength. Next, window openings were defined in the handle wafer with photolithography and 1 µm silicon oxide was removed by reactive ion etching. Without breaking the vacuum, the Bosch DRIE process was utilized to release THz metadevices. Both buried oxide and residuals of silicon oxide mask are left on the sample after etching.

Angle-resolved THz system: Two fiber-coupled terahertz antennas are used as a transmitter and detector (See Figure S5 in the Supporting information). The antennas are mounted on two guide rails that can rotate concentrically with the rotator. The rotator controls the detection angle of the THz beam. The THz wave emitted from the transmitter is collimated by the lens to deliver a nearly collimated beam with a diameter of 5 mm. The samples are placed at the center of the rotator. The deflected terahertz beam is collected by a lens and received by the detector. The detection angle relative to the incident normal varied from -30° to 30° with a step of 2° for the membrane deflector measurements.

THz near-field scanning system: The terahertz wave is emitted from a photoconductive antenna and then it is collected by a parabolic mirror (See Figure S6 in the Supporting information). The samples are excited by a nearly uniform THz beam with a diameter of 5 mm at the normal incidence. The fiber-coupled THz near-field probe with a resolution of 20 μm is mounted on a two-dimensional translation stage which enables two-dimensional field scans. For the electric field profile in the *x*-*z* plane, we scan it with 0.2 mm steps in the *x*-direction from −3.5 mm to +3.5 mm, while the step in the z-direction is 0.5 mm. For the scans in the *x*-*y* plane, the steps are 0.25 mm in both *x* and *y*-directions, with the total span from −3.5 mm to +3.5 mm.

Supporting Information

Supporting Information is available from the Wiley Online Library or from the author.

Acknowledgments The authors thank Dr. Mingkai Liu for helpful discussions, and also acknowledge the use of the Australian National Fabrication Facility (ANFF) at the ACT Node. The work has been supported by the Australian Research Council and the Strategic Fund of the Australian National University. A portion of this research was conducted at the Center for Nanophase Materials Sciences, which is a DOE Office of Science User Facility. The authors also acknowledge support from the Singapore Ministry of Education AcRF Tier 1, Grant RG191/17.

Conflict of Interest

The authors declare no conflict of interest.

Keywords: Mie resonance, All-dielectric, Metasurface, Membrane, Terahertz

Received: ((will be filled in by the editorial staff))
Revised: ((will be filled in by the editorial staff))
Published online: ((will be filled in by the editorial staff))

References

[1] N. I. Zheludev, Y. S. Kivshar, *Nat. Mater.* **2012**, 11, 917.
[2] D. Lin, P. Fan, E. Hasman, M. L. Brongersma, *Science* **2014**, 345, 298.
[3] J. R. Ong, H. S. Chu, V. H. Chen, A. Y. Zhu, P. Genevet, *Opt. Lett.* **2017**, 42, 2639.
[4] I. Staude, J. Schilling, *Nat. Photon.* **2017**, 11, 274.
[5] Y. Yang, I. I. Kravchenko, D. P. Briggs, J. Valentine, *Nat. Comm.* **2014**, 5, 5753.
[6] S. Wang, P. C. Wu, V.-C. Su, Y.-C. Lai, C. Hung Chu, J.-W. Chen, S.-H. Lu, J. Chen, B. Xu, C.-H. Kuan, T. Li, S. Zhu, D. P. Tsai, *Nat. Comm.* **2017**, 8, 187.
[7] Q. Wang, Q. Xu, X. Zhang, C. Tian, Y. Xu, J. Gu, Z. Tian, C. Ouyang, X. Zhang, J. Han, W. Zhang, *ACS Photon.* **2018**, 5, 599.
[8] Q. Yang, X. Chen, Q. Xu, C. Tian, Y. Xu, L. Cong, X. Zhang, Y. Li, C. Zhang, X. Zhang, J. Han, W. Zhang, *Photonics Res.* **2018**, 6, 1056.
[9] S. Sun, Q. He, J. Hao, S. Xiao, L. Zhou, *Adv. opt. photonics* **2019**, 11, 380.
[10] N. Yu, P. Genevet, M. A. Kats, F. Aieta, J.-P. Tetienne, F. Capasso, Z. Gaburro, *Science* **2011**, 334, 333.
[11] J. Li, S. Chen, H. Yang, J. Li, P. Yu, H. Cheng, C. Gu, H.-T. Chen, J. Tian, *Adv. Func. Mater.* **2015**, 25, 704.
[12] T. T. Lv, Y. X. Li, H. F. Ma, Z. Zhu, Z. P. Li, C. Y. Guan, J. H. Shi, H. Zhang, T. J. Cui, *Sci. Rep.* **2016**, 6, 23186.
[13] Y. Xiang, X. Dai, J. Guo, H. Zhang, S. Wen, D. Tang, *Sci. Rep.* **2014**, 4, 5483.
[14] J. Shi, Z. Li, D. K. Sang, Y. Xiang, J. Li, S. Zhang, H. Zhang, *J. Mater. Chem.* **2018**, 6, 1291.
[15] A. I. Kuznetsov, A. E. Miroshnichenko, Y. H. Fu, J. Zhang, B. Luk'yanchuk, *Sci. Rep.* **2012**, 2, 492.
[16] A. I. Kuznetsov, A. E. Miroshnichenko, M. L. Brongersma, Y. S. Kivshar, B. Luk'yanchuk, *Science* **2016**, 354, aag2472.
[17] S. Kruk, Y. Kivshar, *ACS Photon.* **2017**, 4, 2638.
[18] K. Fan, J. Y. Suen, X. Liu, W. J. Padilla, *Optica* **2017**, 4, 601.
[19] L. Wang, S. Kruk, H. Tang, T. Li, I. Kravchenko, D. N. Neshev, Y. S. Kivshar, *Optica* **2016**, 3, 1504.
[20] S. Kruk, B. Hopkins, I. I. Kravchenko, A. Miroshnichenko, D. N. Neshev, Y. S. Kivshar, *APL Photon.* **2016**, 1, 030801.
[21] K. Wang, J. G. Titchener, S. S. Kruk, L. Xu, H.-P. Chung, M. Parry, I. I. Kravchenko, Y.-H. Chen, A. S. Solntsev, Y. S. Kivshar, D. N. Neshev, A. A. Sukhorukov, *Science* **2018**, 361, 1104.
[22] A. Tittl, A. Leitis, M. Liu, F. Yesilkoy, D.-Y. Choi, D. N. Neshev, Y. S. Kivshar, H. Altug, *Science* **2018**, 360, 1105.
[23] M. Decker, I. Staude, M. Falkner, J. Dominguez, D. N. Neshev, I. Brener, T. Pertsch, Y. S. Kivshar, *Adv. Opt. Mater.* **2015**, 3, 813.
[24] K. Fan, J. Zhang, X. Liu, G.-F. Zhang, R. D. Averitt, W. J. Padilla, *Adv. Mater.* **2018**, 30, 1800278.
[25] M. Liu, D.-Y. Choi, *Nano Lett.* **2018**, 18, 8062.

[26] W. Zhou, D. Zhao, Y.-C. Shuai, H. Yang, S. Chuwongin, A. Chadha, J.-H. Seo, K. X. Wang, V. Liu, Z. Ma, S. Fan, *Prog. Quant. Electronics* **2014**, 38, 1.
[27] W. Suh, S. Fan, *Appl. Phys. Lett.* **2004**, 84, 4905.
[28] A. Mekis, J. C. Chen, I. Kurland, S. Fan, P. R. Villeneuve, J. D. Joannopoulos, *Phys. Rev. Lett.* **1996**, 77, 3787.
[29] P. Qiao, W. Yang, C. J. Chang-Hasnain, *Adv. Opt. Photon.* **2018**, 10, 180.
[30] S.-G. Park, K. Lee, D. Han, J. Ahn, K.-H. Jeong, *Appl. Phys. Lett.* **2014**, 105, 091101.
[31] S. Yuan, X. Qiu, C. Cui, L. Zhu, Y. Wang, Y. Li, J. Song, Q. Huang, J. Xia, *ACS Nano* **2017**, 11, 10704.
[32] P. Grahn, A. Shevchenko, M. Kaivola, *New J. Phys* **2012**, 14, 093033.

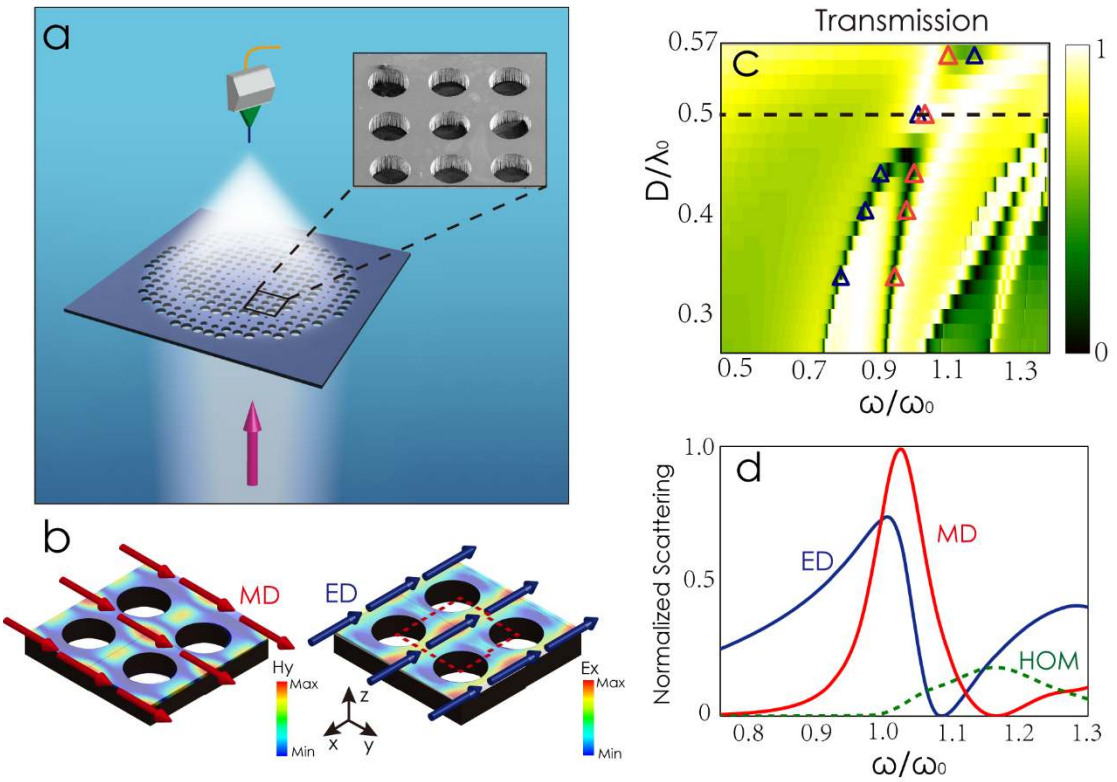

Figure 1. Concept and properties of Mie-resonant membrane metasurfaces**.** (a) Conceptual illustration of Huygens' metasurface based on the ultrathin perforated dielectric membrane. Inset shows the electron microscope image of the fabricated membrane metasurface. (b) The field distribution of MD (blue arrow) and ED (red arrow) of membrane metasurface. The red dashed square denotes the unit cell of a silicon membrane. The thickness of the silicon membrane is deeply sub-wavelength. (c) The transmission profile of the silicon membrane versus the diameter of holes. The red and blue triangle represents the corresponding ED and MD decomposition. Here, ω_0 and λ_0 represent the target frequency and wavelength, respectively. (d) Total multipole contributions of ED, MD resonances and sum of high order multipole (HOM).

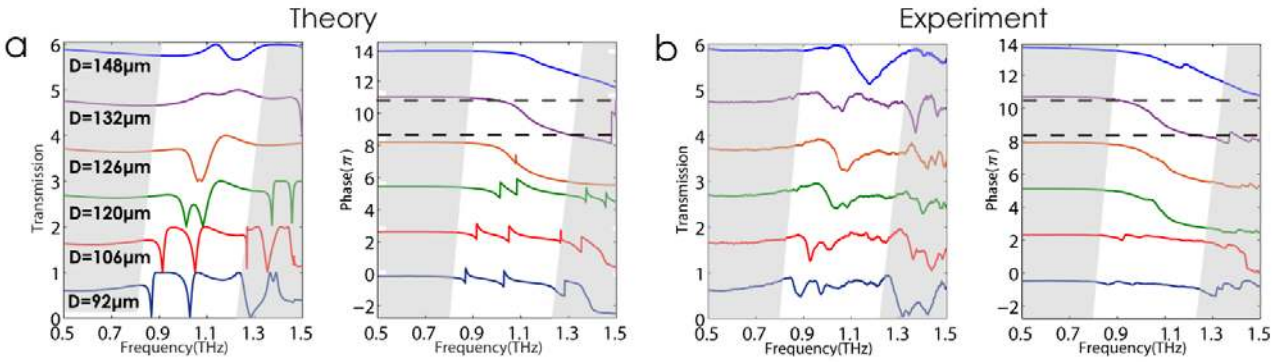

Figure 2. Simulated and measured transmission and phase profiles. (a) Calculated transmission and phase distribution of membrane metasurfaces with different diameters marked next to the curves. (b) Measured transmission and phase profile of the membrane metasurfaces.

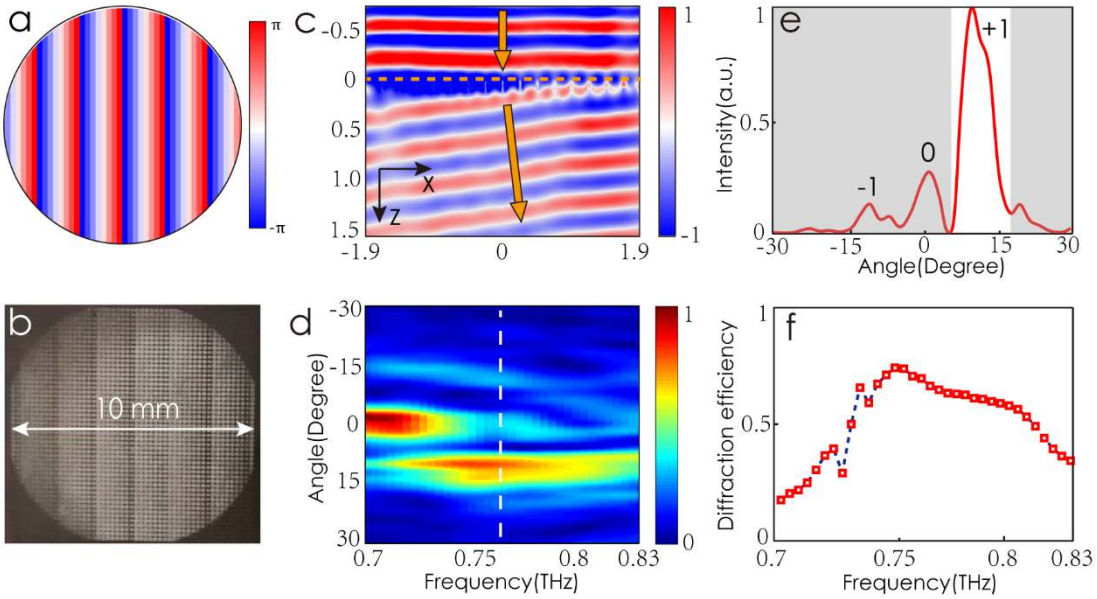

Figure 3. Wavefront control with a membrane deflector. (a, b) Phase profile and optical image of proposed membrane deflector. (c) Simulated electric field distributions of membrane deflector at 0.77 THz. The unit is mm. (d) Measured angle-resolved transmission spectra of beam deflector. (e) Measured angle-dependent output intensity at 0.77 THz. The bright zone denotes the designed diffraction order. (f) The measured diffraction efficiency of membrane deflector.

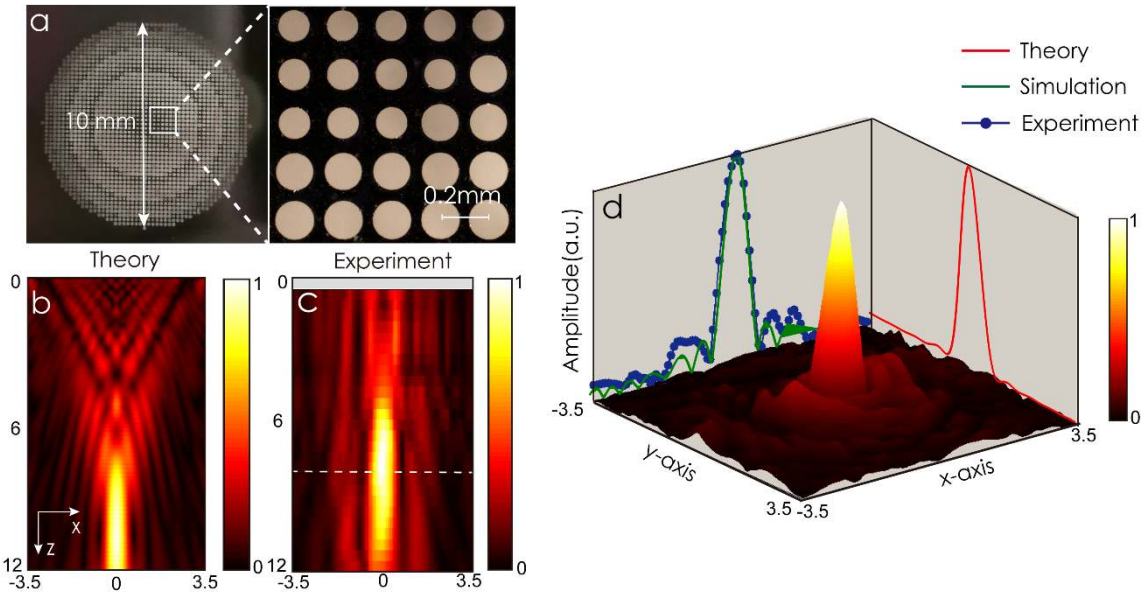

Figure 4. Membrane metalens. (a) Optical image of meta-lens. The Inset of a is the partial enlarge image of membrane lens. (b, c) Simulated (0.77 THz) and measured (0.79 THz) electric field profile of membrane lens at the *x*-*z* plane. The unit is mm. (d) Measured electric amplitudes of the focal plane. The 2D plots on the side are the calculated (red), simulated (green) and measured (blue) cross-section of the electric field profile along the *x*-axis.

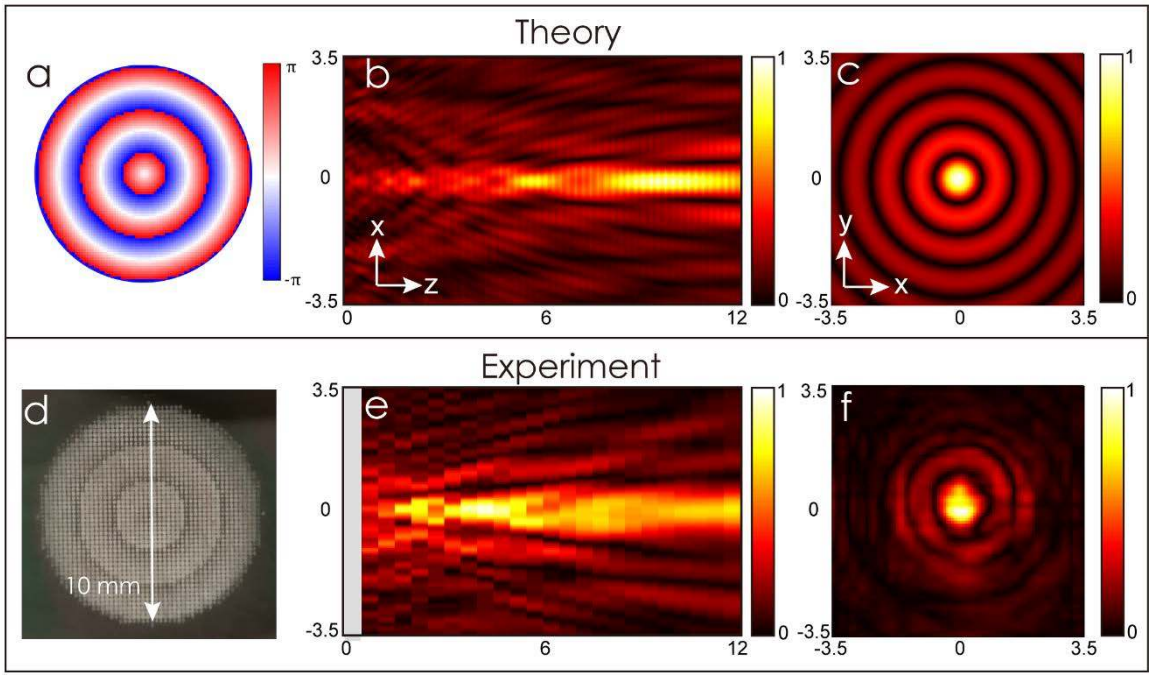

Figure 5. Membrane meta-axicon. (a, d) Phase profile and optical image of proposed meta-axicons.(b, e) Simulated (0.77 THz) and measured (0.83 THz) electric field profile of membrane axicons at the *x*-*z* plane. The unit is mm. (c, f) Calculated and measured cross-section of electric amplitudes at z = 10 mm.